II

X-ray emission from stellar wind driven bubbles: the prototypical UltraCompact H II region, G29.96-0.02

We investigate the missing X-ray emission from stellar wind bubbles in H II regions. Ultra Compact H II regions are unique laboratories to study the interaction of stellar winds with its surroundings; in particular we focus our study on G29.96-0.02 because it is so well-studied at all wavelengths. We address all aspects of UC H II regions: the characteristics of the ionizing star and the energetics involved in the stellar winds, the dynamics of the region and its evolution and expansion. We conduct a broad study, combining X-ray observations of the hot gas with a spectroscopic study of the properties of the ionizing star, and a hydrodynamical study of the dynamical evolution of these regions. We obtained *H*- and *L*-band spectra of the central star of G29.96-0.02 using the ISAAC instrument. Combined with the *K*-band spectrum from Martín-Hernández et al. (2003), we have selected five stellar emission and absorption lines to constrain the stellar parameters. We use a genetic algorithm on the lines to constrain the mass-loss properties of G29.96-0.02. We observed G29.96-0.02 with Chandra X-ray Observatory and found that the hard X-ray emission comes primarily from the star and that it is atypical for single O stars. Furthermore, we found some evidence for a diffuse X-ray component in the soft X-ray band, but no detection for a diffuse hard component. We carried out three-dimensional hydrodynamic numerical simulations using FLASH HC code to understand the dynamics of the region: bow shock, modified champagne flow and modified champagne flow with mass loading. We compare these dynamical studies with observations: we use the radio emission to compare the overall morphology, [Ne II] 12.8 μm line emission to understand the dynamics of the gas and X-rays to unravel the hot gas temperature. We find that champagne flow models are best at explaining the morphology and the gas dynamics, and that mass loading is necessary to cool the shocked stellar wind gas by one order of magnitude to match the X-ray observations.

Silvia Verdolini, Milan Raicevic, Frank Tramper, Arjan Bik, Alex de Koter, Leisa K. Townsley, Patrick S. Broos, Eric D. Feigelson, Alexander G. G. M. Tielens

to be submitted

2.1 Introduction

Recent observations of X-ray emission from H II regions have shed new light on the driving mechanism of H II region evolution. On one hand, compact H II regions like the Orion Nebula and M 17 are associated with diffuse soft X-ray emission at 10^7 K plasma temperatures on parsec scales (Townsley et al. 2003, Güdel et al. 2008, Townsley et al. 2011). This emission is attributed to shocked OB winds which fill bubbles in the molecular cloud. The classical 'Strömgren sphere' of 10,000 K gas is a 'Strömgren shell' on the periphery of these bubbles. On the other hand, the earlier stages of UltraCompact (UC) H II region evolution, with one possible exception (Tsujimoto et al. 2006), show no indication of hot diffuse plasma (e.g., Broos et al. 2007, Oskinova et al. 2010).

The failure to detect hard X-rays from UC H II regions is puzzling. Standard theory of OB stars requires the acceleration of strong winds by resonant coupling of photospheric ultraviolet radiation to an extended atmosphere driving mass loss rates of 10^{-4}-10^{-6} $M_\odot$ yr^{-1} with terminal wind velocities of 1000-2000 km s^{-1} (Castor et al. 1975). These winds sweep up surrounding molecular cloud material. This causes a reverse shock propagating into the wind, resulting in plasmas with temperatures of 10^7-10^8 K and X-ray luminosities of $\geq 10^{34}$ erg s^{-1} (Weaver et al. 1977, van Buren et al. 1990, Harper-Clark & Murray 2009, Arthur 2012). This hard X-ray emission is not observed even at much lower luminosity levels. The absence of hard X-rays might be due to blowout into the turbulent cloud (Mac Low et al. 2007), or shocks weakened by conduction (Weaver et al. 1977, Cowie & McKee 1977, Arthur 2012), mass loading (Hartquist et al. 1986, Pittard et al. 2001b,a), turbulent layers with strong magnetic fields (Kahn & Breitschwerdt 1990), or efficient grain cooling (van Buren et al. 1990). Existing hydrodynamical models of UC H II regions generally treat low energy radiation to model champagne flows or radio morphologies, but do not model in detail the high energy X-rays expected from shocked stellar winds with these effects.

The present paper examines the prototypical and well-studied UC H II region G29.96-0.02 (hereafter G29.96) based on two new observational constraints. First we measure the stellar photosphere and wind properties from near-infrared spectroscopy, finding a spectral type of O5-O6 with $\dot{M} \sim 7 \times 10^{-6}$ $M_\odot$ yr^{-1}. Second we detect a small number of soft X-ray photons within the UC H II region that can be attributed to a plasma with temperature ~0.3 keV and X-ray luminosity $\sim 6 \times 10^{32}$ erg s^{-1}. No hard X-rays are seen. We then construct three-dimensional hydrodynamical model of the UC H II region including photoionization and wind effects, radiative processes, mass loading, and bow shock from stellar motion through the cloud. Viable mass loaded models with realistic radio morphology and [Ne II] 12.8 μm emission line champagne outflow, and with sufficiently weak hard X-ray emission are obtained. The model predictions could be confirmed with deeper X-ray observations.

The rest of this paper is organized as follows. We describe the source G29.96 in Section 2.2. In Section 2.3, we present our new high resolution infrared spectroscopy of the star to determine the mass loss rate and characteristic of the stellar wind and X-ray observations showing a soft diffuse emission indicating a temperature of the gas inside the H II region of about few 10^6 K. In Section 2.4, we describe the numerical method

used in our hydrodynamical calculations that we apply in Section 2.5 and compare to observations in Section 2.6. We conclude in Section 2.7.

2.2 The prototypical UltraCompact H II region: G29.96-0.02

G29.96 is a typical cometary UC H II region, one of the brightest sources at 2 cm wavelength. The cometary shape was first observed by Wood & Churchwell (1989) at radio wavelengths; it is characterized by a bright arc of emission at the head trailing off into a low-surface brightness tail (see Figure 2.1). It is at a distance of 6.2 kpc (Russeil et al. 2011) with a size of ~ 0.15 pc.

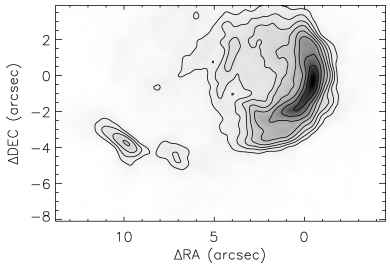

Figure 2.1 – 2 cm continuum map Fey et al. (1995) as readapted by Zhu et al. (2008). The (0,0) position correspond to the peak emission of the [Ne II] line. Contours represent 70%, 50%, 35%, 25%, 17.5%, 12.5%, 9% and 6% of the maximum value in the map.

Zhu et al. (2005) and Zhu et al. (2008) used [Ne II] 12.8 μm fine-structure line mapping as a tool to examine a large sample of compact and UC H II regions with a range of shape and sizes, including G29.96 (see Figure 2.2). The small thermal width of the neon line and the high dynamic range of the maps provide a unique view of the kinematics of UC H II regions. The channel maps show a morphology change from a thin arc-like structure in the blueshifted channels to a cometary shape (as seen in radio) at the molecular cloud velocity to a thicker arc-like structure in redshifted channels.

G29.96 is embedded in a molecular cloud that produces ~ 15 magnitudes of visual extinction (Martín-Hernández et al. 2002). Just in front of the edge of the H II region at about two arcsec east there is a well studied hot molecular core that is probably not heated by the ionizing star of G29.96, but by a young, deeply embedded massive star currently forming in it. Molecular transitions of NH_3 (Cesaroni et al. 1994) and mid-infrared high angular resolution images (De Buizer et al. 2002) showed that the hot core is characterized by small structures (~ 0.1 pc), with kinetic temperatures greater than 50 K and up to 200 K, densities approximating 10^7 cm^{-3}, and masses of a couple hundred solar masses. The region around G29.96 is a star forming complex that contains a filament seen in absorption with *Spitzer* with multiple massive cores (Pillai et al. 2011, Beltran et al. 2013). Using a detailed photoionization model of G29.96 Morisset et al. (2002) found

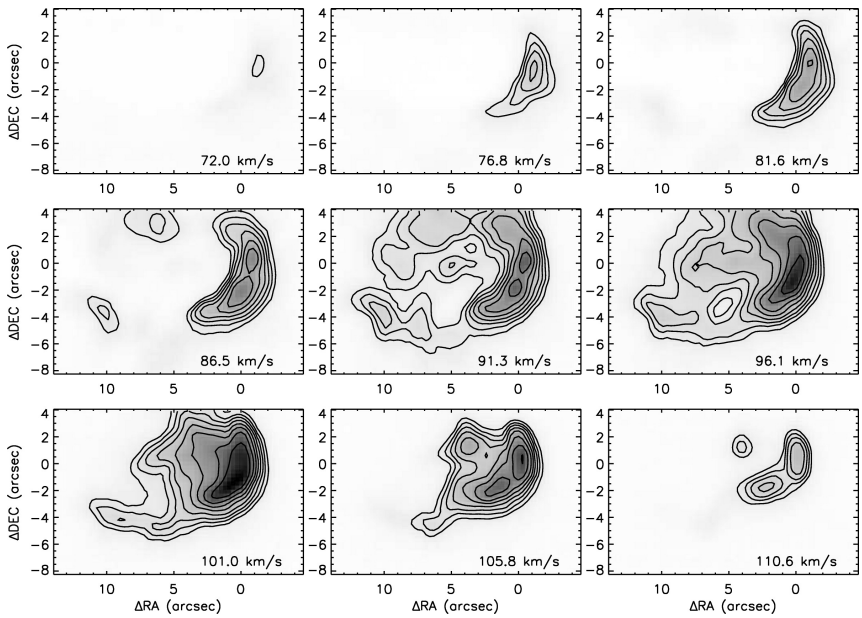

Figure 2.2 – Channel maps of [Ne II] line observations (Zhu et al. 2008). The individual maps sample a single velocity slice in the data cube, representing a width equal to about 4 kms^{-1}. Contours are drawn at 70%, 50%, 35%, 25%, 17.5%, 12.5%, 9%, and 6% of the maximum value of all channels. The molecular cloud velocity is V_{LSR} =98 kms^{-1}.

that the radio and infrared data on G29.96 are best reproduced using a nebular model with two density components: a diffuse ($n_e \sim 680$ cm^{-3}) extended (∼1 pc) component surrounding a compact (∼ 0.1 pc) dense ($n_e \sim 57\,000$ cm^{-3}) core. G29.96 seems to be associated with a small cluster of stars (Fey et al. 1995, Watson et al. 1997, Pratap et al. 1999). The main ionizing star is located in the focus of the bright arc. The first spectroscopic observations by Watson & Hanson (1997) constrained its spectral type to O5V-O8V. Better spectroscopic observations provided a refinement of the spectral type of O5V-O6V (Martín-Hernández et al. 2003), consistent with other observational constraints on the effective temperature of the central star.

Including the new observations presented in this paper, all the important parameters of the source G29.96 are well constrained. The radio image illustrates the morphology of the ionized gas (Figure 2.1). The presence of a hot core in front of the radio arc-structure indicates that the H II region is expanding in a high density medium, with a density distribution typical of a molecular cloud on scales of ∼ 0.1 pc. The near-infrared observations of the effective temperature, the surface gravity and the characteristics of the stellar wind. The [Ne II] line emission reveals the dynamics of the ionized gas, that can be compared with the gas hydrodynamics of the simulations. Finally X-ray observations measure the presence and characteristics of hot gas inside the H II region, directly probing the interaction of the ionizing star and its wind with its surroundings.

Since first discovered, a number of models have been suggested in the literature to explain UC H II region: bow shock (Tenorio-Tagle 1979), champagne flow (Mac Low et al. 1991), turbulence (Peters et al. 2010), and mass loading (Dyson et al. 1995). In view of more recent observations of the source G29.96, the first two models seems preferred for this source. Indeed, Arthur & Hoare (2006) conducted a numerical study testing the bow shock and champagne flow models and combinations of the two models. They suggested that the best fit is reproduced by a combination of the two classical models: a star with a stellar wind moving though a medium (bow shock) with a density gradient (champagne flow).

We present in this work tailored three-dimensional simulations aimed at disentangling the interaction mechanisms between stellar wind and surrounding medium in the specific case of G29.96. We show that both bow shock and champagne flow models predict the presence of hot gas inside the H II region, that is not observed. To solve this problem, we introduce mass loading from photo evaporation or ablation in the hot gas. In a series of papers Dyson et al. (1995), Redman et al. (1996), Williams et al. (1996) proposed mass loading in order to explain the lifetime problem and the shape at radio wavelength of UC H II regions. They use the spatial distribution of the proplyd around the star to (artificially) create the morphology of the region. Instead we assume radial symmetry of the proplyds and explore whether mass loading can reproduce the temperature of the hot gas, as observed in X-ray.

2.3 Observations

2.3.1 IR observation of the star and its wind

2.3.1.1 *H*- and *L*-band spectra

We obtained *H*- and *L*-band spectra of the central star of G29 using the ISAAC instrument (Moorwood et al. 1998), mounted at UT1 of ESO's *Very Large Telescope* (VLT) on Paranal, Chile. The observations where performed in service mode with the *H*-band observations executed on April 14, 2009. The *L*-band data are split in 4 observations and were obtained on August 27, September 23 and October 1st 2009.

The medium resolution setting in combination with a narrow slit (0.3″) was used to obtain a resolution of R=10,000 for the *H*-band spectrum and R=6,700 in the case of the *L*-band spectrum. The spectral setting for the *H*-band observations covers the wavelength range 1.669 μm to 1.748 μm, while the *L*-band spectra cover the wavelength range from 3.858 - 4.124 μm. After each science observations a standard star (HD 181939) of spectral type A0V, using the same instrument settings, was executed. For both datasets, a nodding offset of 25″ was applied as well as a small random jitter of 3″ to allow a sky subtraction without contamination of the surrounding nebular emission of the UC H II region. For the *H*-band a Detector Integration Time (DIT) of 300 seconds per frame was chosen. Four nod cycles (8 frames) were used to take the final spectrum resulting in a total integration time of 40 minutes. In the *L*-band, the sky background is much brighter, therefore a short DIT is required in order not to saturate the sky background. For the *L*-band observations

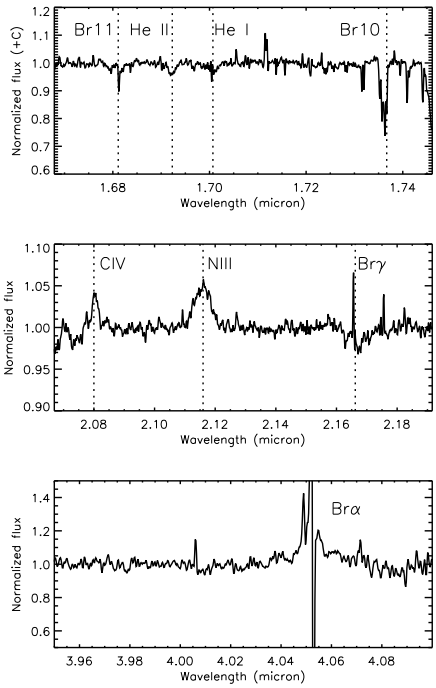

Figure 2.3 – *H*- , *K*- and *L*-band spectra of the central star of G29.96.

we chose a DIT of 5 sec with NDIT = 31, such that each frame is saved after averaging 31 observations of 5 sec. In total we applied 32 nodding cycles split over 4 observing blocks to acquire the final spectrum. The total integration time for the *L*-band spectrum is 3 hours and 26 min.

2.3.1.2 Data reduction

The spectroscopic data are reduced using the ESO pipeline for ISAAC version 6.1.2 in combination with Gasgano. The *H*-band data are corrected using dark and flat field frames taken the morning after the respective observations. The wavelength calibration of the *H*-band data is performed using Ar and Xe arc spectra. After that the final 2-dimensional spectrum was constructed by applying all the calibration files and subtracting the offset positions for the sky subtraction.

For the *L*-band spectra, the wavelength calibration frames were providing a different wavelength solution for each observation, even though the observations were all taken with the same central wavelength. In order to improve the wavelength calibration, we constructed the final two-dimensional spectrum by applying the dark, flat and subtraction of the background first. After that the spectrum was extracted, the 5 emission lines (Hy-

drogen, He I) from the H II region were identified covering the entire observed range of the spectrum. Using their known wavelengths, a 2nd order polynomial fit was performed to derive a wavelength solution for the observed spectra. This results in all the four observations on the same wavelength scale and allows the combination of the entire *L*-band dataset.

The 1-dimensional spectra are extracted using the iraf task *doslit* and combined to a final spectrum (Figure 2.3). Nebular emission is subtracted using a median average in the cross-dispersion direction. This resulted in reducing the contribution of the H II region to a minimum, but not all the emission could be subtracted due to variations of the nebular emission on the slit. When extracting the *H*-band spectra, it turned out that half of the frames had a large detector artifact on the position where the spectrum of the central star was placed. This artifact covered one of the lines of interest for this paper (He I, 1.7007 μm). To recover this line we re-reduced the spectra using only half the dataset and extracted the spectra of half of the frames, resulting a spectrum with a usable He I line.

The standard star observations for both the *H*-band and *L*-band are reduced identical to the science observations. As the standard star is of spectral type A0V, its *H*-band spectrum also has hydrogen lines. These lines are removed by fitting them with a gaussian profile, resulting in a atmospheric transmission spectrum at the airmass of the science observations. The telluric lines are finally removed using the iraf task *telluric*. For the *L*-band observations we decided not to apply the telluric correction as the Br α line is the only line used and is not affected by any telluric absorption.

As additional dataset, we use the *K*-band spectrum (2.068 - 2.192 μm) from Martín-Hernández et al. (2003). We re-reduced the spectrum using the latest version of the ESO pipeline and corrected for nebular contamination in a identical way as the *H*-band spectrum. The final reduced spectra are plotted in Figure 2.3.

2.3.1.3 Mass loss rate

We use the genetic algorithm method developed by Mokiem et al. (2005) to constrain the mass-loss properties of G29.96. This method fits synthetic line profiles produced by the non-LTE atmosphere code FASTWIND (Puls et al. 2005) to observed spectral lines. The most important properties that are constrained by the fits are the effective temperature $T_{\rm eff}$, surface gravity $\log g$ and the mass-loss rate $\dot{M}$. Errors on the derived parameters are calculated as described by Tramper et al. (2011).

To constrain the mass-loss properties of G29.96, we use the observed Br 11, He II λ16923, He I λ17007, Br γ and Br α lines. The resulting best-fit parameters are $T_{\rm eff} = 39.8^{+7.6}_{-1.9}$ kK, $\log g = 3.66^{+0.28}_{-0.16}$ and $\log \dot{M} = -5.15^{+0.1}_{-0.2}$ $M_\odot$ yr^{-1}. Although the mass-loss sensitive lines suffer severely from nebular contamination, the mass-loss rate can, in this particular case of a strong wind, still be constrained by fitting the line wings. Figure 2.4 shows the best-fit Br α line profile, as well as profiles for the 95% probability boundary values.

Given the spectral type O5.5 (Martín-Hernández et al. 2002), we can derived stellar parameters from Martins et al. (2005): effective temperature is 40,000 K, luminosity $\log(L/\,L_\odot)$ is 5.41, and mass is 34.17 $M_\odot$. The empirical mass-loss rate recipe of Vink

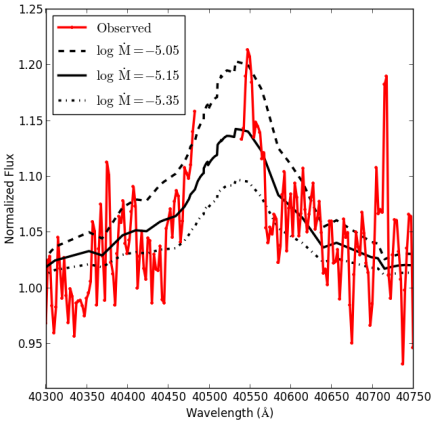

Figure 2.4 – Observed Br α emission with overplotted the best fit model (black solid line) and models for the 95% probability boundary values of $\dot{M}$ (dashed and dashed-dotted lines). Nebular contamination has been clipped from the observed spectrum.

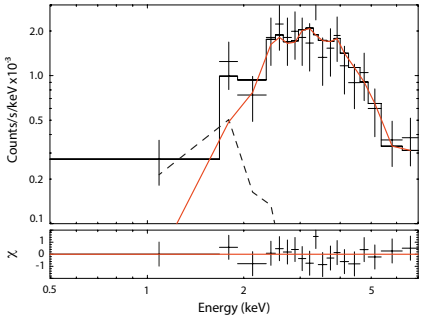

Figure 2.5 – ACIS spectra of G29.96. Stellar component with full line and diffuse component with dashed line.

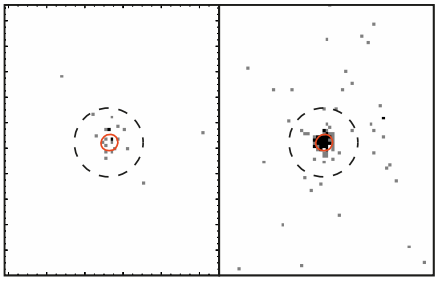

Figure 2.6 – X-ray image of G29.96: 0.5-2 keV events on the left and 2-8 keV on the right. The small aperture has a radius of 2.7 arcsec and contains the diffuse component; the big aperture (dashed line) AE extraction polygon encloses 83% of the O-star PSF.

et al. (2000) would predict a mass-loss rate $\log \dot{M} = -6.08^{+0.28}_{-0.03}$ $M_\odot yr^{-1}$ depending on the terminal velocity assumed. We adopt values of the terminal wind velocity ranging from 1000 to 3000 km s^{-1}. Such empirical value is about eight times lower than our derived value with FASTWIND models. However considering the uncertainties in the derivation of the spectral type and the approximations of the Vink et al. (2000) empirical recipe, we can consider the ionizing star a normal O5.5-O6 star with a typical mass-loss rate. Consistently, we assume that the terminal wind velocity has a typical value of 2000 km s^{-1}.

Table 2.1 – X-ray luminosity and surface brightness. We assume a distance of 6.2 kpc (Russeil et al. 2011).

		Soft (0.5-2 keV)	Hard (2-8 keV)
Observations			
Star (inner 1.31 arcsec^2)	L_X (erg s^{-1})	2.4×10^{33}	1.2×10^{33}
Annular region (diffuse)	L_X (erg s^{-1})	6.7×10^{32}	6.0×10^{31}
	S_b (erg s^{-1} arcsec^{-2})	3.1×10^{31}	2.8×10^{30}
Champagne Flow Simulations			
no mass loading	L_X (erg s^{-1})	5.9×10^{32}	7.8×10^{32}
with mass loading	L_X (erg s^{-1})	2.1×10^{32}	5.7×10^{32}

2.3.2 X-ray observations

G29.96 was observed by the Chandra X-ray Observatory using the ACIS Imaging Array in 2009 February, for 27.5 ks. The aimpoint of the telescope was placed on the UC H II region, to achieve the highest spatial resolution and sensitivity possible. A total of 172 X-ray point sources were found across the entire $17' \times 17'$ field of view. Details of this observation are given in Townsley et al 2014 (submitted).

The third-brightest source in the field (with 105 net counts) is the O star ionizing the UC H II region, with an ACIS source name of 184604.07-023921.5 (which defines the coordinates of the X-ray source). The X-ray spectrum of this source is well-fit in *XSPEC* by a simple absorbed thermal plasma, with the model form *tbabs*apec*, with the plasma abundance frozen to solar values (Figure 2.5). The fit gives an absorbing column of $N_H \sim 12\times10^{22}$ cm^{-2} (90% confidence range [8×10^{22}, 1.8×10^{23}]) and a thermal plasma temperature of kT $\sim$ 1.8 keV (90% confidence range [1.2, 3.3] keV). Using a conversion is $N_H \sim 1.6 \times 10^{21} A_V$, our derived N_H amounts to $A_V \sim 75$ mag.

The ionizing star of G29.96 is a hard X-ray source with an X-ray luminosity of 3.5×10^{33} erg s^{-1} (90% confidence range [1.4×10^{33}, 1.3×10^{34}]), see Table 2.1. This hard X-ray emission is atypical for single O stars, and likely indicates that it is a colliding-wind binary and/or has a substantial magnetic field.

The observed stellar X-ray luminosity represents only a small fraction ($\simeq 4\times10^{-4}$) of the mechanical luminosity of the star and, hence, whatever process converts wind kinetic energy into X-ray, it is not very efficient. We note that the column density of absorbing gas is much larger than the gas column density associated with the dust absorbing the H II region (A_V ~15 mag, Martín-Hernández et al. 2002). Hence, much of the X-ray absorbing column is associated with the stellar wind, reinforcing that only a small portion of the wind had been converted into hot, X-ray emitting gas.

We performed two concentric extractions of the X-ray data, within an *inner* region (dashed line polygon in Figure 2.6) and the *outer* region (full line circle in Figure 2.6). We are interested in the photometry of the annular region between the *outer* and *inner*

region, which we will refer to as the *annular* extraction. The annular extraction has two background components: the wings of the PSF of the star, and the large-scale 'flat' background. The number of counts expected from the wings of the star can be calculated using the fraction of the PSF enclosed by the inner aperture, which is energy dependent. We have direct measurements of this PSF fraction at 1.5 and 4.5 keV. The 1.5 keV value is suitable for the soft band; for the hard band we estimate a PSF fraction at the median energy of the events in that band (3.5 keV) by interpolating between the two measurements. We find that the annular region contains very little wing contamination in the soft band (∼1 count), but significant contamination in the hard band (∼32 counts). The number of counts expected from the large-scale "flat" background (instrumental and astrophysical) can be estimated using a hand-drawn background region – 382 times larger than the red aperture – that avoids other detected point sources and areas with off-nominal exposure time. In summary, the data indicate an excess of 12.6±3.77 counts in the soft band that could be attributed to diffuse X-ray emission, and 6.13±7.01 counts in the hard band (i.e. consistent with a null detection). As in all massive star-forming regions, there may be a population of unresolved low-mass stars near the O star that would complicate interpretation of the "diffuse" emission.

We use the program PIMMS[1] NASA/GSFC HEASARC (first described in Mukai (1993)) to derive the intrinsic luminosity of the soft components. We use the APEC plasma model with adopted temperature kT=3.4 keV (T = 4×10^7 K, see Section 2.5) and an absorbing gas column corresponding to A_V ∼15 mag. We summarize the luminosity found for the diffuse component in Table 2.1. We also calculate the intrinsic surface brightness of the diffuse components by dividing by the area of the annulus (∼ 2.6 arcsec^2) to consistently compare with a plasma that uniformly fill the entire radio UC H II region (Figure 2.5).

In conclusion, there is no evidence for an extended hard X-ray component down to a limit of 1.6×10^{31} erg s^{-1} for an adopted plasma temperature of kT=3.4 keV (see above for assumptions). We do find some evidence for a diffuse component of about 12.6 counts in the soft X-ray band indicating a plasma temperature of ∼0.3 keV.

2.4 Numerical method

We use the code FLASH HC, a modified version of the FLASH code (Fryxell et al. 2000) extended with a Hybrid Characteristics radiative transfer scheme developed by Rijkhorst et al. (2006). The FLASH code is a block-structured, adaptive mesh refinement (AMR) hydrodynamics code with modular design and scalable to tens of thousands of processors. The Hybrid Characteristics (hereafter HC) is a ray-tracing radiative transfer scheme designed specifically with FLASH block structure in mind. To obtain the intensity at each simulation cell, column densities along rays that connect each cell with a source of radiation are computed. Total column density in one such ray is obtained by adding the contribution of each block intersected by the ray, which is in turn interpolated from ray

[1] http://heasarc.gsfc.nasa.gov/Tools/w3pimms.html

segments precomputed on each block. The use of interpolation eliminates the overhead associated with recomputing column densities in neighbouring rays. On the other hand, limiting the interpolation to the coarse, block level minimizes numeric diffusion that can be caused by it. This makes the HC scheme both highly efficient and precise. Furthermore, the algorithm is highly parallel, as most of the work is performed independently on each block as intended by FLASH design. We have made several improvements to the HC scheme since its introduction by Rijkhorst et al. (2006), some of which have already been described in Raicevic (2010) and one will be detailed here[2]. We present tests of the code in Appendix 2.8. The updated version of the scheme was employed in the radiative transfer code comparison project by Iliev et al. (2009).

2.4.1 New approach to find blocks cut by a ray

One of the steps of the hybrid characteristic method is finding all the blocks that are cut by a single ray, which is a non-trivial problem since the blocks are distributed among different processors. Rijkhorst et al. (2006) solved this problem by representing the whole block structure using a uniform grid array stored on each processor, with the resolution corresponding to the highest refinement level of the AMR grid. The list of block cut by each ray is then obtained by tracing the ray over this helper array. Unfortunately, the fact that the helper array is itself not distributed among processors makes it a memory bottleneck, artificially limiting the highest refinement level the AMR structure can reach. One solution for this problem was presented by Peters et al. (2010) who removed the helper array and instead used a custom function that finds the list of cut block by walking the AMR tree structure. We use a very similar approach to theirs, with the difference that the crux of our implementation is a function already present in the FLASH code's particle module which reports the global block number for a point placed anywhere within the simulation volume. Starting at the beginning of each ray, we move a point along it and query the tree structure through the aforementioned function to obtained the list of cut blocks. The point is moved in steps of size of the last block found, in order to avoid unnecessary queries. This new approach finds the same lists of cut blocks as the original one while significantly reducing the memory cost of ray tracing, which is crucial for achieving high enough spatial resolution of the AMR grid needed for physical problems of our interest.

2.4.2 Changes to the chemistry solver

The biggest change to the HC scheme introduced in Raicevic (2010) was the update of the chemistry equation solver, which was redesigned to guarantee photon conservation in respect of both spatial and temporal discretization. As shown in Abel et al. (1999), in order for the photo-ionization rate Γ_{ph} not to depend on the spatial size of the volume elements in a simulation volume, it should be set directly to correspond to the number of photons that is absorbed by the volume element. Assuming a hydrogen-only medium:

[2] The code is available upon email request.

$$\Gamma_{\rm ph} \propto \frac{N_{\gamma,\rm in}(1-e^{-\Delta\tau})}{N_{\rm HI}}, \tag{2.1}$$

where $N_{\gamma,\rm in}$ is the number of photons entering the volume element, $\Delta\tau$ is its optical depth and $N_{\rm HI}$ is the number of neutral hydrogen atoms found in the element. Both $\Delta\tau$ and $N_{\rm HI}$ are linear functions of the hydrogen neutral fraction of the volume element, $x_{\rm HI}$. We adopted the version of Eq. 2.1 photoionization rate as formulated in Mellema et al. (2006). Assuming that the time step is short enough that $x_{\rm HI}$ remains constant in all volume elements, this formulation will guarantee the correct number of ionizations in the simulation volume irrespective of the spatial resolution. However, ensuring this criterion usually requires extremely short time steps, which makes the RT component of a simulation by far the most expensive. The need for short time steps can be significantly relaxed if the chemistry solver takes into account the change of $x_{\rm HI}$ during a time step, as shown in Mellema et al. (2006). Due to the change of the neutral fraction in the simulation volume during a longer time step, both $N_{\gamma,\rm in}$ (which is a description of the total column density between the volume element and the source) and $x_{\rm HI}$ (which describes the column density within the volume element itself) are not constant. In order to take these changes into account, Mellema et al. (2006) used a short characteristics ray tracing scheme to construct rays in an outward manner starting from the source and using the time-averaged optical depths of individual cells. The way that the volume elements are crossed in the scheme allow it to automatically take the change in $N_{\gamma,\rm in}$ into account, but makes the parallelization of the algorithm difficult.

Due to the highly parallel nature of the HC algorithm, it is impossible to adapt it to the Mellema et al. (2006) prescription which depends on the order of cell crossings. However, we can take into account the changes of the neutral fraction $x_{\rm HI}$ *within the volume element* with little effort. In Raicevic (2010), it was shown that just that is enough to correctly track D-type ionization front using several orders of magnitude longer time steps than before possible. In order to make this possible, we replaced the originally used DORIC solver (Frank & Mellema 1994), which solves the chemistry equations in an efficient manner by iterating on their analytic solutions, by the Livermore Solver for Ordinary Differential Equations (LSODE, Hindmarsh 1980) with which we directly integrate the same equations taking into account the time dependence of $x_{\rm HI}$. While the new solver is significantly less efficient than the original one, the ability to employ much longer time steps for the whole RT calculation makes the change worthwhile.

2.4.3 Cooling

For the cooling rate, we use a sum of collisional ionization, collisional excitation, recombinations and Bremsstrahlung cooling rates (Theuns et al. 1998). We added Oxygen cooling lines. See Table 2.2.

Table 2.2 – Cooling rates (ergs $cm^{-3}s^{-1}$) of the elements considered. We adopt the following nomenclature: $T_n \equiv T/(10^n \text{ K})$ with T in K; H I = $n_{\text{H I}}/n_{\text{H}}$, where $n_{\text{H I}}$ is the density of neutral hydrogen and n_{H} is the total hydrogen density; H II = $n_{\text{H II}}/n_{\text{H}}$, where $n_{\text{H II}}$ is the density of ionized hydrogen; n_e is the number of free electrons; and g_f is the Gaunt factor.

Cooling	Approx	El.
Collisional ionization	$c_1 = 2.54 \times 10^{-21} T^{1/2} \exp(-157809.1/T)(1 + T_5^{1/2})^{-1} n_e \text{H I}$	H I
Recombination	$c_4 = 8.7 \times 10^{-27} T^{1/2} T_3^{-0.2} (1 + T_6^{0.7})^{-1} n_e \text{H II}$	H II
Collisional excitation	$c_8 = 7.5 \times 10^{-19} \exp(-118348/T)(1 + T_5^{1/2})^{-1} n_e \text{H I}$	H I
Bremsstrahlung	$c_{10} = 1.42 \times 10^{-27} g_f T^{1/2} n_e \text{H II}$ $g_f = 1.1 + 0.34 \exp\{-[(5.5 - \log_{10} T)^2]/3\}$	H II
Line emission	$c_{\text{O III}} = 5 \times 10^{-23} (n_e \text{H II})^2 T_4^{1/2} \exp(-29000/T)$	[O III]
Line emission	$c_{\text{O I}} = 2.5 \times 10^{-29} (n_e / \text{H II})^2 T^{0.67} \exp(-228/T)$	[O I]

2.4.4 Stellar winds

The stellar wind is implemented in the simulation as a source term centered in a region around the location of the star. At each time step our modified version of `hydro_sweep` function restores the wind conditions in the wind source region. Even though the stellar wind region is part of the computational domain, effectively it behaves as an inflow boundary. We chose the optimal radius of the stellar wind generator, that satisfy both requirement of being small enough that the stellar wind reaches its terminal velocity outside the wind generator region and large enough that the spherical surface can be resolved reasonably well in cartesian coordinates. We always use the highest refinement level around the star source term to make sure it is as spherical as possible at all times.

At each time step, we set the density of the wind ρ_w the temperature of the wind T_w and the radial velocity of the stellar wind v_w in the wind generator region. We assume a stellar wind velocity $v_w = 2000$ km s^{-1}, and we derive density and temperature of the wind from the mass loss rate $\dot{M}$ as follows:

$$\rho_w = \frac{\dot{M}}{4\pi v_w R_\star^2}, \tag{2.2}$$

$$T = \frac{\mu m_{\text{H}} v_w^2}{3k}, \tag{2.3}$$

where $R_\star$ is the radius of the star, that in our simulations corresponds to the radius of the source term, in general some orders of magnitude bigger that the actual star radius; ρ_w and T_w are respectively the density and temperature of the wind, k is the Boltzmann

constant, μ is the mean mass per particle and $m_{\rm H}$ the mass of a hydrogen atom. We have assumed that the velocity of the wind is close to the expansion velocity of an adiabatic gas into vacuum. From Eq. 2.2 and Eq. 2.3 we can derive the density of the wind, ρ_w, and an approximate value for the temperature of the wind, T_w. We also give the gas in the stellar wind source terms a radial velocity equal to the stellar wind terminal velocity.

2.4.5 Star moving

We simulate the movement of the star as the medium moving in the opposite direction and we keep the star position fixed. In this way we avoid waste of computation time in recalculating the movement of the grid. We give a bulk velocity along the positive x-axis to the ambient material at the initial time step. We set the negative x-boundary as an inflow boundary with material going in at the velocity of the star $v_\star$.

2.4.6 Mass loading

With mass loading we refer to the general idea that the injection of mass in the wind will cool it down, making it invisible in X-rays. Mass loading occurs when gas from embedded clumps is stripped away and injected in the surrounding medium. The mechanism of injection of mass into the medium can be photoionization or hydrodynamic ablation.

The aim of this paper is to understand the effects of mass injection in shaping and determining the energy budget of the UC H II region, therefore we assume that mass loading happens as a localized injection of mass that we artificially include in the simulations. At this point we are not interested in understanding which of the mechanisms is responsible for the mass loading. We implement mass loading as localized sources of mass, such as proplyds in Orion nebulae. Henney & Arthur (1998) model the volume density of proplyd in Orion as

$$\rho_p(D) = \frac{\rho_0}{(1 + D^2/D_0^2)^\alpha}, \tag{2.4}$$

where D is the distance from the source, D_0 the inner radius within which there are no proplyds, ρ_0 is the central stellar density and α=1.29 is a parameter derived from observations of Orion. By assuming that the proplyd fraction f_p as a function of the projected radius d depends only on the parameter α and that the proplyd and stellar profiles have the same ρ_0 and D_0, they derive

$$f_p(D) = \frac{\Gamma(\alpha - 1/2)}{\sqrt{\pi}\Gamma(\alpha)} \left[1 + \left(\frac{d}{D_0}\right)^2\right]^{1-\alpha}, \tag{2.5}$$

where Γ is usual gamma function.

We randomly pick the radial positions of each clump using Eq. 2.5, so that the resulting distribution follows Eq. 2.4. Besides location, every clump is the same: it is characterized by a radius, a mass loss rate and a velocity of the gas injected. Numerically we implemented it in the same way as we did for the stellar wind. Given mass loss rate and velocity of the gas lost we derive density and temperature of the gas injected (similar

Table 2.3 – Fiducial parameters

Star parameters	
Type	O5.5
$\mathbb{N}_{Lyc}$	$8.5{\times}10^{48}$ s^{-1}
Stellar wind	
$\dot{M}$	7×10^{-6} M$_\odot$ yr^{-1}
v_w	2000 km s^{-1}
$R_\star$	4×10^{16} cm
Star moving	
$v_\star$	20 km s^{-1}

Mass Loading distribution of clumps	
number of clumps	50
D_0	$\sim 6 \times 10^{16}$ cm
α	1.29
Mass Loading gas injection	
$\dot{M}_c$	10^{-6} M$_\odot$ yr^{-1}
R_c	5×10^{15} cm
v_c	10 km s^{-1}

to Eq. 2.2 and 2.3). Since proplyds are gravitationally bound we do not change their location during the simulation.

2.5 G29.96: simulations

We carry out three dimensional simulations aimed at explaining the observed morphology and dynamics of G29.96. We follow the Arthur & Hoare (2006) study and carry out three models: bow shock model, modified champagne flow model (ionizing star with stellar wind in a medium with a density gradient), and the addition of mass loading on the modified champagne flow model. We present numerical models of the three theoretical scenarios in three-dimensions with initial parameters suitable for G29.96 as derived from observations.

2.5.1 Bow shock model

The source of ionizing photons is assumed to move in a uniform medium of density $5{\times}10^4$ cm^{-3} and velocity 10 km s^{-1}. The box is 1 pc in each direction. The maximum refinement level is 6, with smallest refined element being ~0.01 pc. The source is kept steady in the computational box, and the medium is moving at the velocity of the star. The stellar wind is launched from a spherical region of radius 0.013 pc around the location of the star.

In Figure 2.7 and 2.8 top row, we show the number density, velocity field, temperature and ionization front after 10,000 yr and 20,000 yr from the start of the simulation. At the beginning of the simulation the ionization front expands up to the Strömgren radius, 0.02 pc, on a recombination timescale 1.3 yr. Later, the ionization front is taken over by the stellar wind that shocks the gas heating it up, and sweeps up a dense thin shell of neutral material, in which the ionization front is trapped. As the swept-up shell expands, the stellar wind creates a reverse shock with the shocked gas at a radius of ~0.05 pc. The result is a stratified structure similar to the Castor et al. (1975) solution. Close to the star there is the free-flowing new stellar wind material that has a density of about 10 cm^{-3} and

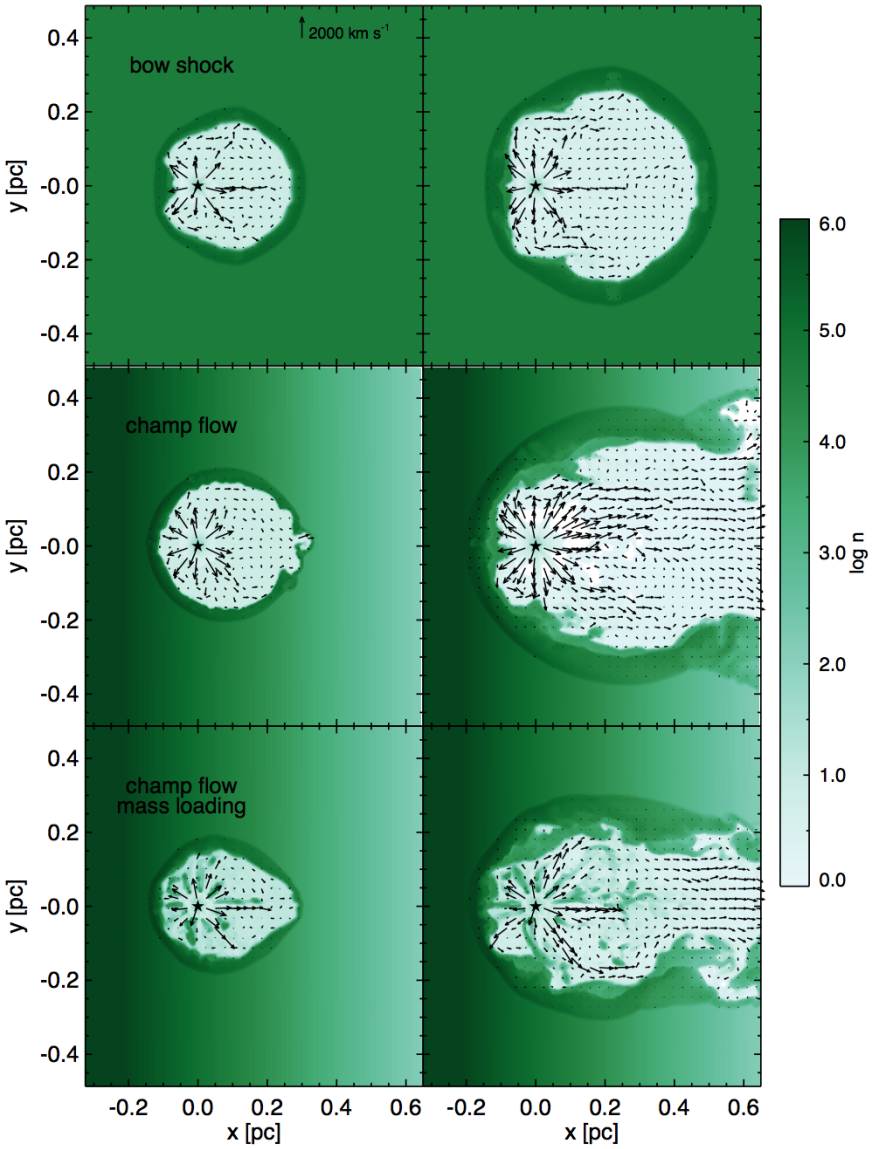

Figure 2.7 – Number density (in cm^{-3}) together with the velocity field (in $km\,s^{-1}$) for the bow shock model (top row), the modified champagne flow (middle row), and modified champagne flow model with mass loading (bottom row) at age 10,000 yr (left column), and 20,000 yr (right column) of a slice of 3D simulations through the location of the source. In the bow shock model the medium is uniform and the star moves through it. For the other two models the star is not moving and the density profile has a gradient.

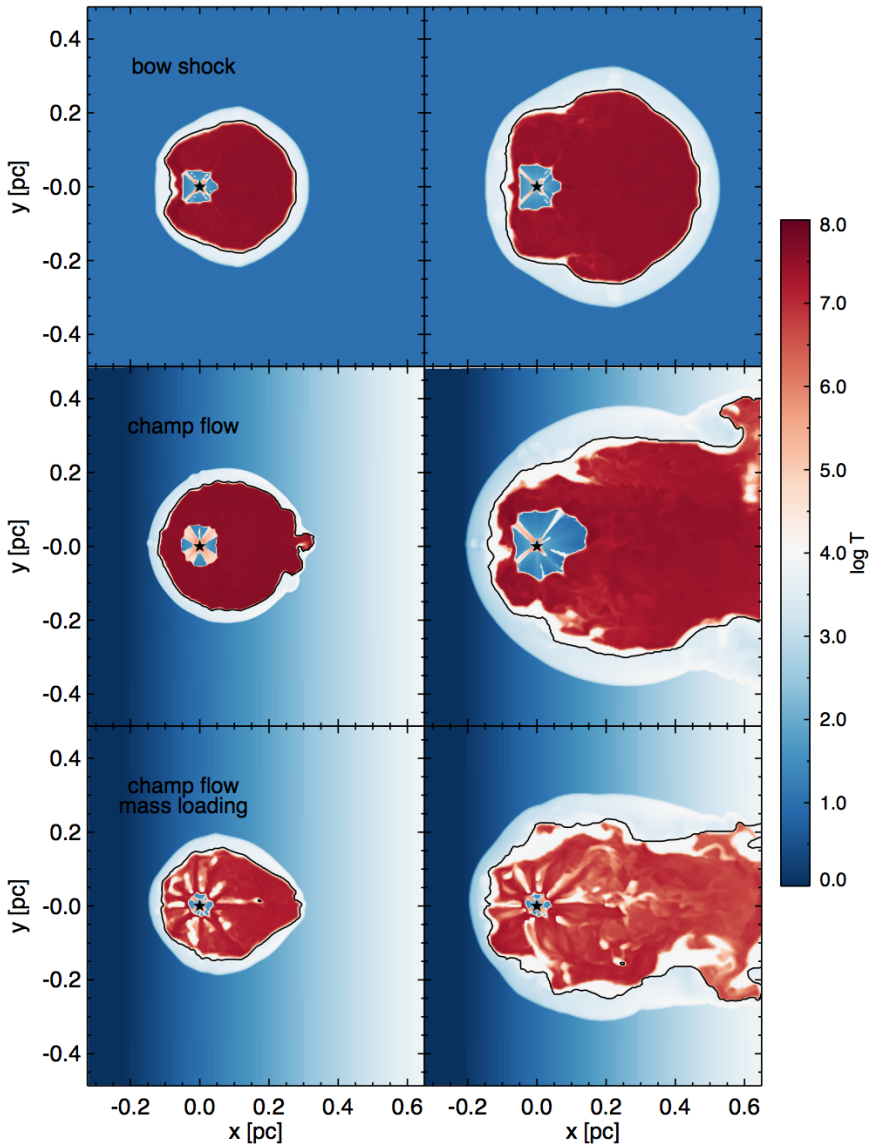

Figure 2.8 – Gas temperature (in K) together with the ionization front (marked in black) for the bow shock model (top row), the modified champagne flow (middle row), and modified champagne flow model with mass loading (bottom row) at age 10,000 yr (left column), and 20,000 yr (right column) of a slice of 3D simulations through the location of the source.

temperature 100 K, the amount of thermal pressure injected by the star is fixed, and as the gas expands radially, the volume occupied increases and density and temperature drop consequently. The free-flowing stellar wind is separated from the shocked stellar wind gas by the reverse shock. The shocked gas has a temperature up to $4{\times}10^7$ K and density of 10 cm^{-3}. The contact discontinuity divides the shocked hot gas from the swept-up and photoionized gas that has a density of about 1000 cm^{-3} and temperature 10^4 K. The shell of ionized gas extends up to the ionization front that is trapped inside the swept-up shell of neutral material with density up to 10^6 cm^{-3} and temperatures of few hundred Kelvin.

The movement of the star through the medium creates the bow shock that at an early phase is an elongate sphere with the star located offset from the center. At age 20,000 yr, the star is completely offset in the H II region and gas is flowing from head to tail. The swept-up material is located in a thick dense shell that does not break up before leaving the box. Indeed, the high density of the medium prevents this to happen, and such a high density is needed to keep the size of the region as small as observed (0.2-0.3 pc in radius).

The shocked stellar wind gas is turbulent, primarily due to Rayleigh-Taylor instabilities creating at first the typical mushroom hat shape and then evolve into more chaotic motions along two vortices. It is particularly visible at the head of the region, where gas with high pressure is pushed by the stellar wind into the medium and against the ram pressure due to the movement of the star. The instability sets up at the beginning of the simulation, creating a mushroom-like shape. At a later stage, the instability propagates and becomes Kelvin-Helmholtz unstable as the gas moves along the walls of the H II region.

2.5.2 Modified champagne flow model

We set up an ionizing star at fixed location with a stellar wind in a medium with a density gradient that follows an exponential profile $n = n_0 \exp(x/H)$, where n_0 is the density at the location of the star, equal to 5×10^4 cm^{-3} and H is the scale height set equal to 0.1 pc.

In Figure 2.7 and 2.8 middle row, we show the number density, temperature and ionization fraction after 10,000 yr and 20,000 yr from the start of the simulation. As in the case of the bow shock simulation, the overall structure consists of a free-flowing stellar wind region, hot shocked stellar wind, ionized gas shell and swept-up dense neutral material. Since the medium is not uniform the ionized region is not a sphere, the H II region expands further to the low density side creating an egg-like shape.

After 10,000 yr the H II region breaks open towards the low density side. The ionization front is trapped in the swept-up shell of the stellar wind. At the tail of the region, the swept-up shell is thinner than at the head. With time the swept-up shell becomes progressively thinner till the point where thin shell instabilities start to take place. Those instabilities corrugate the shell and facilitate the shell to break up and photons to escape (see Appendix 2.8 for more details on the thin shell instability). The shocked gas inside the bubble is at about $\sim 4 \times 10^7$ K. At 20,000 yr, the H II region is completely open and the ionized gas accelerates and escapes, and the ionization front penetrates deeper into the swept-up shell. As in the case of the bow shock model, Rayleight-Taylor instabilities dominate inside the hot bubble, making it turbulent.

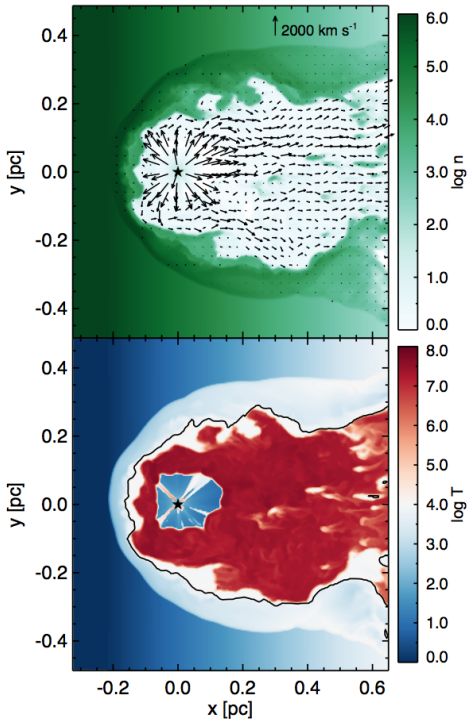

Figure 2.9 – Number density (in cm^{-3}) together with the velocity field (in $km\,s^{-1}$) (top), and gas temperature (in K) with ionization front marked in black (bottom) for the modified champagne flow model with mass loading after 5,000 yr from the full evaporation of all proplyd of a slice of the 3D simulation through the location of the source.

2.5.3 Modified champagne flow with mass loading

In Section 2.6, we explain why the bow shock model is not in good agreement with the observation characteristics of G29.96, while the modified champagne flow model can reproduce all the observations but the X-rays. This is due to the high temperatures of the gas inside the bubble as caused by the reverse shock. Therefore, we introduce mass loading from photo evaporating proplyds to the modified champagne flow only, our preferred model. The addition of gas inside the bubble will lower its temperature. We study here the typical temperatures that can be reached.

We run the champagne flow model, as described in Section 2.5.2, with the addition of a population of proplyds that are photo evaporating (as described in Section 2.4.6). We consider a population of proplyd as found in Orion and with mass loss rates typical of

photo evaporation processes.

Figure 2.7 and 2.8, bottom row, show the results of including mass loading in the champagne flow model. When compared with the original models (Figure 2.7 and 2.8, middle row), it is clear that the overall shape has not changed, but the inside of the bubble has structures due to the additional gas from proplyds that creates a turbulent medium, efficiently mixing cold and hot gas. The average temperature of the gas inside the bubble decreases by about an order of magnitude, while the density increases.

Considering a typical mass of a proplyd of $2{\times}10^{-2}$ $M_\odot$ with constant mass loss rate of 10^{-6} $M_\odot$ yr^{-1}, the lifetime of a proplyd is 20,000 yr. After 20,000 yr all the proplyds should have run out of gas, therefore we continue to run the simulation without mass loading for another 5,000 yr to investigate how long it takes to increase the temperature of the bubble again. Results are shown in Figure 2.9. After 5,000 yr, the gas around the star has reached again the high temperatures of the initial champagne flow model, because all the evaporated gas is transported towards the tail of the region.

2.6 Comparison with observations

In this section we carry on a detailed comparison of out simulations with observations. We compare with the [Ne II] 12.8 μm fine-structure line mapping (Zhu et al. 2008), the 2 cm radio maps (Wood & Churchwell 1989) and the X-ray SED.

2.6.1 Simulated radio emission measure maps

We generate simulated emission measure maps for the radio emission by assuming Bremsstrahlung radiation. First, we rotate rigidly the box around one axis at a given angle, the viewing angle. Then, we pick a line of sight along any of the new axis, depending how we want to project the object. Since our simulations are approximately axis-symmetric along the x-axis cutting through the source, it is interesting to rotate along the y-axis cutting through the source and look at the object head and tail at different viewing angles. After the box rotation, the radio continuum maps are generated by first calculating cell by cell the free-free absorption coefficient at frequency ν (Rybicki & Lightman 1979)

$$\alpha_\nu^{ff} = 3.7 \times 10^8 T^{-0.5} Z^2 n_e^2 \nu^{-3} (1 - \exp(-h\nu/kT)) g_\nu \,, \tag{2.6}$$

where T is the gas temperature, Z is the atomic number, n_e is the electron density, h is the Plank constant, k the Boltzmann constant in cgs, and g_ν is the gaunt factor at frequency ν. The optical depth at distance r is

$$\tau_\nu = \int_0^r \alpha_\nu^{ff} ds. \tag{2.7}$$

We integrate again to find the brightness temperature $T_{b\nu}$ as

$$T_{b\nu} = \int_0^\tau T e^{-\tau_\nu} d\tau_\nu. \tag{2.8}$$

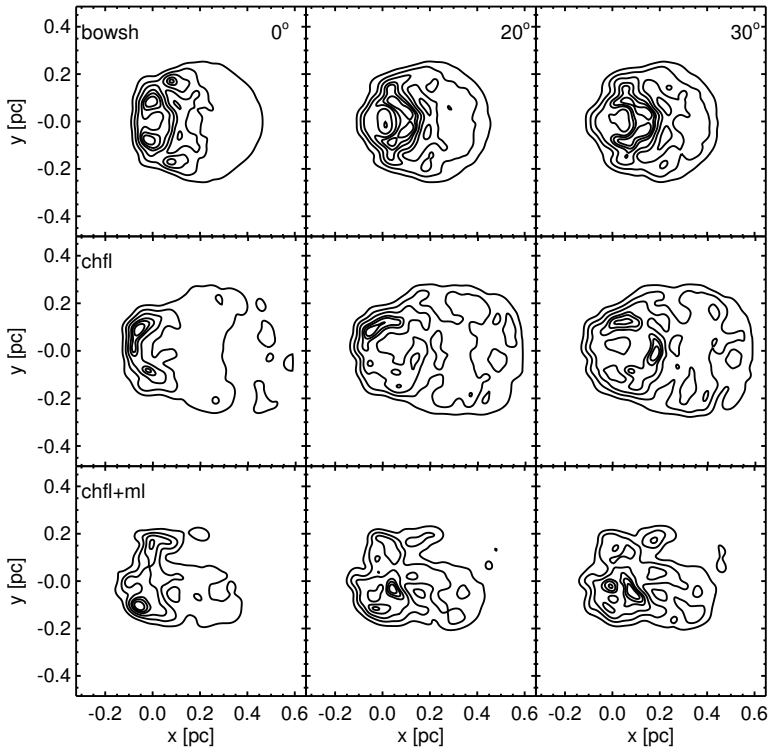

Figure 2.10 – Simulated radio emission measure maps for the three models at age 20,000 yr: bow shock model (top row), champagne flow model (central row), and champagne flow with mass loading model (bottom row). We rotate the source by 0, 20 and 30 degrees (respectively, from left to right columns) rigidly around the y axis and then project onto the plane of the sky.

We finally derive the surface brightness (Mac Low et al. 1991)

$$S = 2 \times 10^{23} k T_{bv} \Omega_{bm} / \lambda^2 \text{ Jy beam}^{-1}, \tag{2.9}$$

where Ω_{bm} is the solid angle subtended by the beam. We then convolve the image with a gaussian with a full-width-half-maximum typical of the radio observations of Wood & Churchwell (1989).

Figure 2.10 shows the radio expected emission of the bow shock, modified champagne flow and modified champagne flow with mass loading model. We change the orientation of the source by 0, 20 and 30 degrees with the head towards the observer. The best models that matches the observations is the champagne flow model that can reproduce the cometary shape of the radio emission (Arthur & Hoare 2006). The head is brighter

and has an arc-like structure, and the extended emission follows the cometary shape of the region. Since the swept-up shell of the bow shock model does not break open, the resulting radio emission is more spherical than arc-like. For this reason, we believe that in the conditions of G29.96 – very high ambient medium density – this model is not appropriate to explain this region. When we introduce mass loading, the region is more turbulent and it is hard to discern the cometary shape.

The orientation of the source with respect to the observer is important for the morphology of the radio emission. We find that the best match is achieved with a very small angle of rotation, about 10 degrees. Arthur & Hoare (2006) suggested an angle of 20 degrees to be the best fit, however, they did not build a model specific for G29.96 and they simply derive the value from trends found in their numerical study. Since the angle is so small and makes little difference to the results, for simplicity, we show the rest of the results without any rotation.

2.6.2 Velocity maps

In order to compare our simulations results with the observation of [Ne II] 12.8 μm fine-structure line mapping (Zhu et al. 2008, Figure 2.2), we create velocity maps as follows. We take the velocity component along the z-axis to be the line of sight velocity, we then divide it in velocity bins. We add a normalized gaussian line profile to account for the thermal broadening of the line, considering the temperature of the simulation. Finally we add a point spread function typical for the observations. Figure 2.11, 2.12 and 2.13 show velocity maps for the bow shock, the modified champagne flow and the champagne flow with mass loading at age 20,000 yr.

The observations (Figure 2.2) show two features in the ionized gas: a clear arc-like structure at the rest frame velocity (98 km s^{-1}), and a somewhat disturbed gas at blue- and red-shifted velocities. In the case of the bow shock, the H II region never breaks open, seen in the velocity maps as a round feature, where the tail is also visible. Therefore, for the case of G29.96 we exclude the bow shock model.

For the other two models we find that, on one hand, the champagne flow model can best reproduce the rest frame arc-like structure, on the other hand, the model with mass loading is able to reproduce the disturbances in the ionized gas at blue- and red-shifted velocities. When mass loading is introduced, the cometary shape is less clear. The injection of gas from proplyds disturbs the dynamics of the region, generating a more turbulent picture. The bright arc-structure is still recognizable at zero velocity, but almost absent in the blue- and red-shifted channels. Both champagne flow models give a good representation of the dynamics of the ionized gas. Observations show that a less turbulent way to mass load the gas would be the best model to explain both arc-like feature and turbulences.

2.6.3 X-ray luminosity and spectral energy distribution

The diffuse soft X-ray emission observed towards G96.96 indicates the presence of a diffuse plasma at a temperature $< 10^6$ K. Both bow shock and modified champagne flow models predict an average temperature of the shocked stellar wind gas of $\sim 5 \times 10^7$ K.

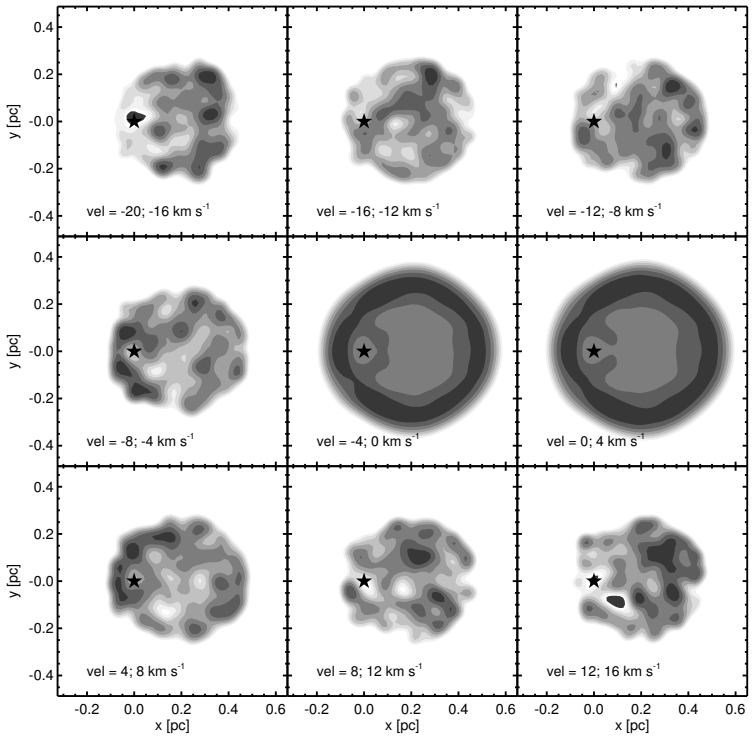

Figure 2.11 – Prediction of velocity bin maps of [Ne II] line observations (Zhu et al. 2008) for the bow shock model at 20,000 yr.

Only when mass loading is included the temperature of the shocked stellar wind gas cools to $\sim 4 \times 10^6$ K. Therefore, mass loading is an efficient way to cool the shocked gas and can explain the observed diffuse soft X-ray emission.

We also calculate the total expected X-ray luminosity by assuming Bremsstrahlung radiation only. We take the emissivity of the Bremsstrahlung, that depends on density and temperature of the gas in the simulation, and integrate over the volume and a frequency range (0.5-8.0 keV) (Sarazin 2009). Results are shown in Table 2.1. We find that, while we are able to explain the diffuse soft X-ray component, we are unable to justify the lack of diffuse hard X-ray emission. However, we did not include the extra cooling in the hot plasma due to the dust. Dust is not contained in the stellar wind, but it might be introduced in the bubble from proplyd evaporation. Therefore, in the model with mass loading and extra cooling can be assumed. Indeed, the presence of dust can enhance the cooling rate up to a factor of 100 for temperatures 10^7-10^8 K (van Buren et al. 1990, Dwek 1987,

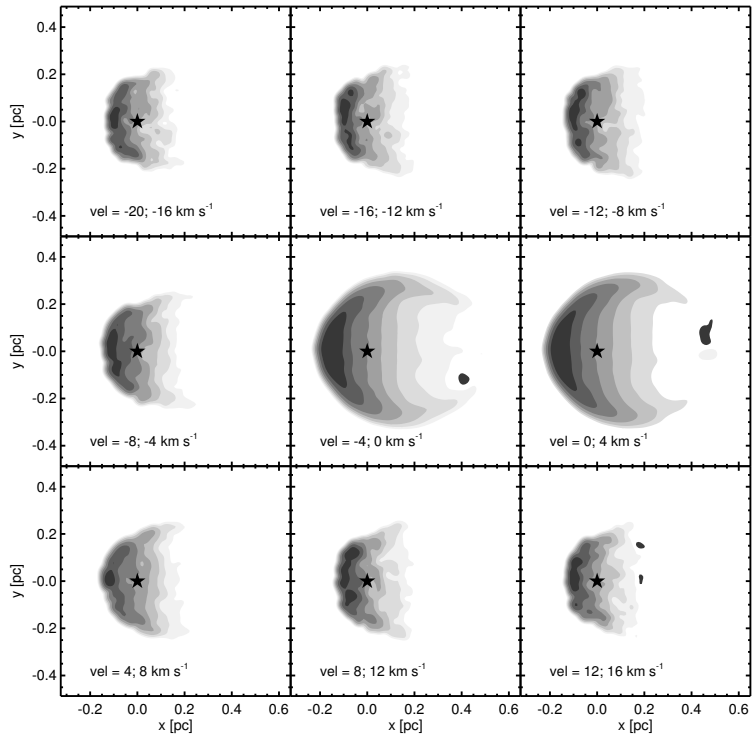

Figure 2.12 – Prediction of velocity bin maps of [Ne II] line observations (Zhu et al. 2008) for the modified champagne flow model at age 20,000 yr.

Everett & Churchwell 2010).

2.6.4 Summary

We carried out three-dimensional numerical simulations aimed at understanding the interaction of the stellar winds with its surroundings for the prototypical cometary UC H II region, G29.96. Radio maps of this source show the morphology of the ionized gas, while [Ne II] line emission maps display the dynamics of the gas. Furthermore, we have constrained the stellar type and the mass loss rate of the ionizing source, indicating a strong stellar wind. Finally, we have detected hard X-rays from the star – either from a colliding wind binary or from a coronal region – and only a small component for diffuse soft X-rays. The latter demonstrates that the plasma in the bubble is not very hot.

With all the parameters constrained by observations, we investigate three models for

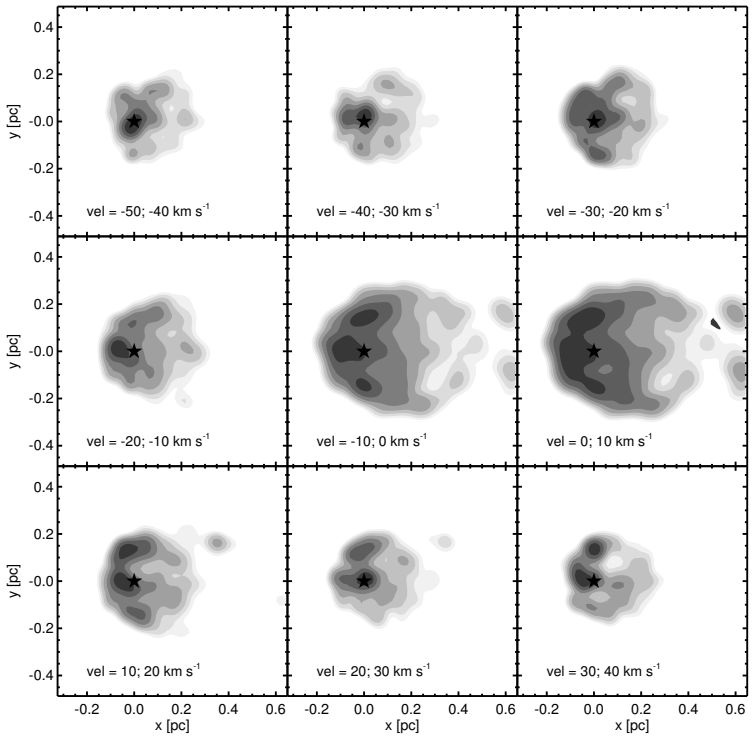

Figure 2.13 – Prediction of velocity bin maps of [Ne II] line observations (Zhu et al. 2008) for the modified champagne flow model with mass loading at age 20,000 yr.

the evolution of the source: bow shock, modified champagne flow and modified champagne flow with mass loading. We exclude the bow shock model because it fails in reproducing both the morphology of the region, as seen in the radio, and the dynamics of the ionized gas, as revealed by the [Ne II] line emission. The only two assumptions in the bow shock model are the velocity of star (10 km s^{-1}), and the density of the uniform medium ($5{\times}10^4 cm^{-3}$). Besides observations indicating that the density in the source surroundings is quite high (Martín-Hernández et al. 2002), we need such a high value for the ambient density to keep the source confined to a small radius. However, the high ambient density also causes the model to not succeed in reproducing the morphology. Indeed, under these conditions the swept-up shell cannot break open at the tail of the region resulting in a different morphology in the radio. Even more telling, the calculated dynamics does not reproduce the [Ne II] velocity maps.

In contrast, the modified champagne flow is able to reproduce both the cometary mor-

phology of G29.96 the radio emission and the velocity maps of [Ne II] line emission showing the typical bright arc structure that fades towards the tail of the region. However, both classical models – bow shock and modified champagne flow – predict intense diffuse soft X-ray emission inconsistent with the observations. Indeed, the shocked stellar wind gas of both models reach temperatures of $\sim 4 \times 10^7$ K, that should have been seen in the soft X-ray band. It indicates that there must be a mechanism at work that cools the shocked stellar wind gas by about one order of magnitude.

We introduced mass loading from proplyd evaporation in the modified champagne flow model. Adopting a reasonable proplyd distribution, the injection of mass in the shocked stellar wind region cools the gas by one order of magnitude and it can explain the X-rays. However, the overall morphology of the region gets so disturbed that the good morphology match we obtain by the modified champagne flow model vanishes.

We conclude that the surrounding core must have a density gradient that generates the cometary shape. We emphasize that the stellar parameters – effective temperature and mass loss rate – are well constrained by our observations. There is some leeway in the adopted density distribution for the surrounding core. However, the density of 5×10^4 cm^{-3} is in good agreement with observation of the ionized gas density (Martín-Hernández et al. 2002). The scale height of the density distribution (0.1 pc) leads to a morphology which is in good quantitative agreement with the observations (cf., Figure 2.1 and 2.10). In addition, this model reproduces the observed velocity field quantitatively (cf., Figure 2.2 and 2.12). However, the classical interaction of stellar winds with the surrounding does not explain the X-ray observations. Mass loading mechanisms are able to lower the temperature of the shocked gas, but proplyd evaporation makes the gas turbulent and prevent the model to explain the morphology of the region. A more regulated mass loading effect must take place, one example could be mass loading from the swept-up gas shell.

2.6.5 Discussion

The large variety of observed UC H II in morphology and kinematics has been explained by various models. Detailed numerical work on the interaction of stellar winds with the ambient medium in the presence of radiation has been carried out by Freyer et al. (2003, 2006) discussing the appearance of thin shell instabilities and their effects on the dynamics. In a broader contest, Arthur & Hoare (2006) explored a combinations of bow shock (van Buren et al. 1990) and champagne flow models (Tenorio-Tagle 1979, Bodenheimer et al. 1979, Yorke et al. 1983) in order to identify the characteristic of each model and their predictions to compare with observations.

We have studied in details the source G29.96 as a prototype of cometary UC H II. For the particular case of G29.96 we excluded bow shock models. However, we emphasize that it does not exclude the validity of this model for other sources. Numerical work has been carried out mostly in the context of runaway stars (Raga et al. 1997, Comeron & Kaper 1998) showing appearance of structures as a result of the interaction between the fast stellar wind of a runaway star and the surroundings, complicated by the presence of magnetic fields (Mackey et al. 2013).

We found that the classical models alone – bow shock, and modified champagne flow

– cannot explain the lack of diffuse soft X-rays observed towards G29.96. Mass loading of the hot plasma is a promising mechanism to cool the hot shocked gas. However, evaporation from proplyds will dominate the morphology and dynamics of the region. As a result, the adopted spatial distribution of the proplyds has to be highly tailored (Dyson et al. 1995) and that is not very realistic. The presence of dust in the hot plasma can enhance the cooling rate as much as a factor of 100 for temperatures $10^7 - 10^8$ K (van Buren et al. 1990, Dwek 1987, Everett & Churchwell 2010). Although stellar winds do not have dust, we can assume that some dust is mixed in the hot gas from proplyd evaporation. In such scenario, the gas can cool more efficiently and less mass loading from proplyds is necessary to lower the temperature by one order of magnitude. Therefore, less dynamical disruptions will happen in the bubble.

Besides the morphology, another problem with mass loading from proplyds is that after a short time all the proplyds in the vicinity of the ionizing star are fully photo evaporated and the shocked gas starts warming up again. In a recent paper, Gritschneder & Burkert (2013) studied the dynamics of proplyds. They consider proplyd formation to happen in the expanding shell of an H II region, as the effect of triggered star formation. Those newborn stars have an initial velocity that tends to push them away from the ionizing star, leaving the H II region free of proplyds. However, Gritschneder & Burkert (2013) show that in high density cases, such as Orion, stars have enough time to be gravitationally pulled back towards the ionizing star. G29.96 is similar to Orion in terms of densities, therefore there is the possibility that proplyds return might keep the hot gas mass loaded and at lower temperatures for longer timescales than considered by us.

Other explanations that could explain the absence of X-rays have been suggested in the past. One is the blowout scenario: the wind kinetic energy mostly stays in the form of kinetic energy rather than thermalizing in a strong shock. This would happen if the volume of turbulent molecular clouds is mostly low-density material, with only small pockets of high density material (Mac Low et al. 2007). However, while this is a reasonable general scenario for the interaction of stars with their surroundings, it is unlikely to be able to explain the observed morphology of this particular source. Another possibility is that mass loading happens at the contact discontinuity through conduction mechanisms: electrons from the hot shocked gas transfer energy to the ionized gas shell, the hot gas cools and mass is injected from the ionized gas into the hot gas. Arthur (2012) studied conduction in unidimensional simulations and found a significant thickening of the ionized gas shell and lower temperatures of the shocked gas. One final suggestion is magnetic turbulent layers: the introduction of magnetic fields into the molecular cloud prior to H II region expansion can lead to thick turbulent mixing layers with lower temperatures at the wind/cloud boundary (Kahn & Breitschwerdt 1990 and Falceta Gonçalves, personal communication).

2.7 Conclusions

We present a broad study of UC H II regions combining X-ray observations of the hot gas with spectroscopic study of the properties of the ionizing star, and a hydrodynamical study

of the evolution of these regions. We focusing our analysis on G26.96, a very well-studied typical UC H II region.

We collected observations of the *H*- and *L*-band spectra of the ionizing star of G29.96. Combined with the *K*-band from Martín-Hernández et al. (2003), we have five emission lines: Br 11, He II λ16923, He I λ17007, Br γ and Br α.

We used the genetic algorithm developed by Mokiem et al. (2005) to fit the observed lines with synthetic line profiles to constrain the mass loss rate. The best-fit parameters are $T_{\rm eff} = 39.8^{+7.6}_{-1.9}$ kK, $\log g = 3.66^{+0.28}_{-0.16}$ and $\log \dot{M} = -5.15^{+0.1}_{-0.2}$ $M_\odot yr^{-1}$.

We observed G96.96 with Chandra X-ray Observatory using ACIS-I. The spectral hardness of the ionizing star of G29.96 shows that the source is not a typical single star, indicating the presence of a colliding-wind binary and/or has a substantial magnetic field. We find some evidence for a soft X-ray diffuse component, but no detection of a diffuse hard component.

We use 3-dimensional hydrodynamic code with radiative transfer to model the UC H II region. We create three models of the expansion and evolution of the H II region. The first one is the bow shock model characterized by an ionizing star with a stellar wind that moves through a uniform density medium. The second one is the modified champagne flow model, where the ionizing star with stellar winds is in a medium with a density gradient. The third model is the second models with the addition of mass loading due to proplyd evaporation.

For each model, we produce observables that we directly compare to observations. From the comparison with the radio maps, we exclude the bow shock model. With the very high densities of the medium required to keep the UC H II region small, the swept-up shell cannot break open, resulting in a shape of the ionized gas too spherical.

Thanks to the X-ray observations, we exclude the modified champagne flow model. Such model predicts the presence of a diffuse component of the soft X-ray, that is not observed. The model that can explain all the simulations at once is the modified champagne flow model with mass loading. Mass loading acts as a coolant of the hot gas of the shocked stellar wind.

2.8 Appendix: Code testing

The FLASH HC code was extensively tested as part of the radiative transfer code comparison project, the Rijkhorst et al. (2006) version used in Iliev et al. (2006) and the updated version we use in this work in Iliev et al. (2009). In this section, we extend those tests with new ones more suited to the high density regimes of interest in this work. We also reproduce the work of Arthur & Hoare (2006) to test our code against a known result for a more detailed stellar wind problem.

Expansion of an H II region in a uniform density medium

The tests performed in the RT code comparison project (Iliev et al. 2006, 2009) focused on physical conditions commonly found in the intergalactic medium, however the condition

in the interstellar medium are very different. Namely, the densities of interest in this work are several orders of magnitude higher than those used for the code comparison tests. In order to confirm that the code is appropriate for use in those density regimes, we perform two test problems with known analytic solutions previously used in the code comparison project.

The first test we perform is the variation on Test 1 from Iliev et al. (2006), which is the expansion of an H II region around a single ionizing radiation source embedded in a static, hydrogen-only uniform density medium. The only difference to the Iliev et al. (2006) test is that we increase the density of the medium, $n_{\rm H}$, by six orders of magnitude, to $n_{\rm H} = 10^3$ cm^{-3}.

There is a well-known analytic solution for the evolution of ionization front radius of the H II region expected in this case, assuming a constant temperature in the gas and infinite photoionization cross-section:

$$r_{\rm I}(t) = \mathcal{R}_{\rm s}(1 - e^{-t/t_{\rm rec}})^{1/3}, \tag{2.10}$$

where $t_{\rm rec} = (\alpha_{\rm B}(T) n_{\rm H})^{-1}$ is the recombination time scale and $\mathcal{R}_{\rm s}$ is the final size of the H II region obtained by equating the number of recombination in the H II region with the number of photons emitted by the source $\mathbb{N}_{Lyc}$, the so called Strömgren radius,

$$\mathcal{R}_{\rm s} = \left(\frac{3\mathbb{N}_{Lyc}}{4\pi\alpha_{\rm B}(T) n_{\rm H}^2} \right)^{1/3}. \tag{2.11}$$

The setup parameters are as follows. The simulation volume is cubical with side dimension $L_{\rm box} = 6.6$ pc. The computational grid used to represent the volume is uniform, with 128 cell per box side. The medium is static, hydrogen-only gas with uniform number density $n_{\rm H} = 10^3$ cm^{-3} and kept at constant temperature $T = 10^4$ K throughout. A source of monochromatic photons of energy $E_\gamma = 13.6$ eV is placed at the corner of the simulation volume, at coordinates $(0, 0, 0)$, and emits $\mathbb{N}_{Lyc} = 5 \times 10^{48}$ photons per second. For these parameters, the recombination time scale is $t_{\rm rec} = 122.31$ years. We run the simulation for 500 years.

In Figure 2.14 we show the position of the ionization front radius as a function of time compared with the analytic solution from Eq. 2.10. The difference with the analytic solution is caused by the fact that the photoionization cross section in our simulation is not infinite, therefore the ionization front in the simulation has a finite thickness and photons can penetrate deeper into the neutral medium than assumed in the analytic solution. This fact was already discussed in Iliev et al. (2006) and our result agrees with the behavior of all codes shown there. We conclude that FLASH HC is able to reproduce the analytic solution for the evolution of an H II region in a static medium in the density regime of interest for our work.

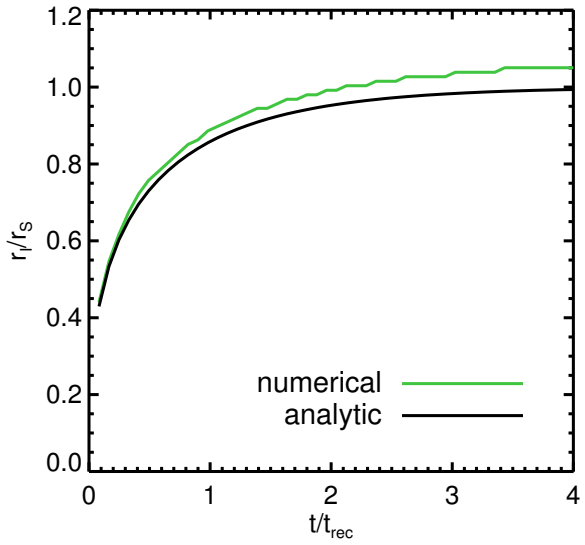

Figure 2.14 – Expansion of the ionization front in uniform medium at fixed temperature. The plot shows in full black line analytic expansion of the radius as a function of time as described in Eq. 2.10; and the numerical results in gray.

Pressure supported expansion of an H II region in a uniform density medium

The second test we perform is a variation on Test 5 from Iliev et al. (2009), which is the classical problem of the expansion of an ionization front due to a single ionizing radiation source embedded in a uniform density medium. As for the previous test, the only difference to the Iliev et al. (2009) test is that we increase the density of the medium, $n_{\rm H}$, by six orders of magnitude, to $n_{\rm H} = 10^3$ cm^{-3}.

We focus our analysis on the evolution of the ionization front after the Strömgren radius has been reached. This first phase happens on a recombination timescale, that is very short compares to the time evolution we want to reach in this work. Once the ionization front has reached the Strömgren radius, the pressure of the ionized gas within it is higher that the pressure of the ambient medium. Such overpressure drives the expansion of the ionization front beyond the Strömgren radius, as predicted by the classical Spitzer (1978) solution:

$$r_I = R_{st}\left(1 + \frac{7c_s t}{4R_{st}}\right)^{4/7} \tag{2.12}$$

where c_s is the sound speed in the ionized gas.

We perform the test with the very similar input parameters as before but with hydro-

dynamic effects included, meaning that the gas is not isothermal. The setup parameters are as follows. The simulation volume is cubical with side dimension $L_{\rm box} = 6.6\,{\rm pc}$. The computational grid is uniform, with 128 cell per box side. The medium has a uniform number density $n_{\rm H} = 10^3\ {\rm cm}^{-3}$ and at initial temperature $T = 10^2\,{\rm K}$. A source of monochromatic photons of energy $E_\gamma = 13.6\,{\rm eV}$ is placed at the corner of the simulation volume, at coordinates $(0, 0, 0)$, and emits $\mathbb{N}_{Lyc} = 5 \times 10^{48}\ {\rm s}^{-1}$. For these parameters, the recombination time scale is $t_{\rm rec} = 122.31\,{\rm yr}$. We run the simulation for 1.5 Myr.

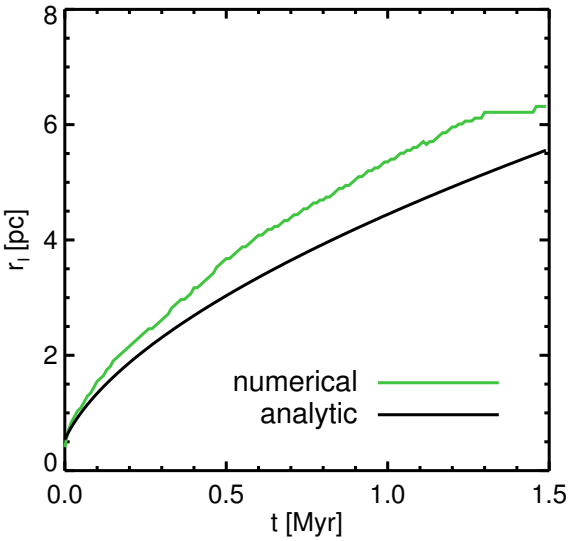

Figure 2.15 – Expansion of the ionization front in uniform medium with hydrodynamic response. The plot shows with black line the analytic expansion of the radius as a function of time as described in Eq. 2.12, and with gray line the numerical result of the simulation.

Figure 2.15 shows the results of the test. We include the Spitzer analytic solution as described in Eq. 2.12 and the numerical test. We find reasonable good agreement throughout the expansion between code and analytic solution. As found by Iliev et al. (2009), the global dynamics of the ionization front at this stage depend primarily on the temperature of the ionized gas that driver the overall expansion.

The H II region radial evolution is overestimated. Iliev et al. (2009) noticed that the analytic solution describes well the early and late evolution of the expansion, but not the intermediate. Furthermore, the radial evolution does not match the $r^{4/7}$ expansion predicted by the analytic solution, but it approaches it at late times as the radius of the front becomes larger, also seen in Iliev et al. (2009). We conclude that FLASH HC reproduces reasonably well the analytic solution for the evolution of an H II region in a non-static medium in the high density regimes.

Stellar wind

The interaction of stellar winds with a medium is a problem that has been studied in many different astrophysical contexts. More recently there has been an interest in studying the interaction of stellar winds with the radiation of the star. In particular, the work of Freyer et al. (2003, 2006) and Arthur & Hoare (2006) explored this in detail. The extensive work done allow us to use such a setting as a test case for our code. As far as we know, the FLASH HC code has never been used in a similar setting, and we want to check the reliability of our code. We set up a test as the Arthur & Hoare (2006) expansion of an H II region in the presence of a stellar wind. The box size is 0.15×0.15 pc with constant density medium 6000 cm^{-3} and temperature 300 K. The ionizing star is located at the corner of the box in the origin of the axis and it is a blackbody of effective temperature 30000 K. We set the mass loss rate is 10^{-6} M$_\odot$ yr^{-1} and terminal wind velocity 2000 km s^{-1}. We performed the same test in both 2D and 3D and at different resolutions. For the sake of comparison with Arthur & Hoare (2006) we show first results of the 2D models. The number density together with the velocity field, the gas temperature, and the degree of hydrogen ionization after 200 and 500 yr from the beginning of the simulation are shown in Figure 2.16(a) and 2.16(b) respectively.

Figure 2.16(a) shows the stellar wind model at age 200 yr. The ionization front moves quickly approximately to the location of the Strömgren radius, $R_{st} \sim 0.07$ pc, in a recombination timescale ~ 1.7 yr. The pressure of the ionized gas is higher than the cold medium causing the ionization front to expand further. This expansion is smaller than the stellar wind but still visible in the small arrows of the velocity field in the outer shell. The stellar wind bubble expands into the ionized and preheated ambient medium. Cooling in the outer shell of swept-up gas is efficient and causes the shell to collapse to a thin layer. Due to thin-shell instability (Vishniac 1983) dense knots are produced along the shell, causing a higher optical depth along rays going thought them. This causes the rippling of the photoionization front, and the shadowing effect visible in the plot. The free-flowing wind is heated by the reverse shock at ~ 0.03 pc to very high temperatures of about 10^8 K.

Figure 2.16(b) shows the evolution at 500 yr. At this stage the thin shell of swept-up gas has reached a radius ~ 0.06 pc and the thin shell instability has evolved in more dense knots and a more perturbed shell. The degree of ionization went from almost 100% to 5% in the region between the initial ionization front and the thin shell due to trapping of the photons by the high dense swept up shell region. Spikes of ionized gas are characteristic of the instability and represent the propagation of the ionization fronts in collimated beams through gaps in the knotty shell.

We further studied the thin-shell instability modes at higher refinement to confirm that they have no influence on the outcome of our simulations. In Figure 2.17(a) and 2.17(b) we present the same stellar wind simulation as above for refinement level 9. Also Freyer et al. (2003) proved that the energy budget is not influenced by the refinement. Comparing Figure 2.16(a) and 2.16(b) with 2.17(a) and 2.17(b) it is possible to see that the location of the ionization front and of the swept-up shell does not change with refinement. As expected, the main change with increasing resolution is the level of details that are found.

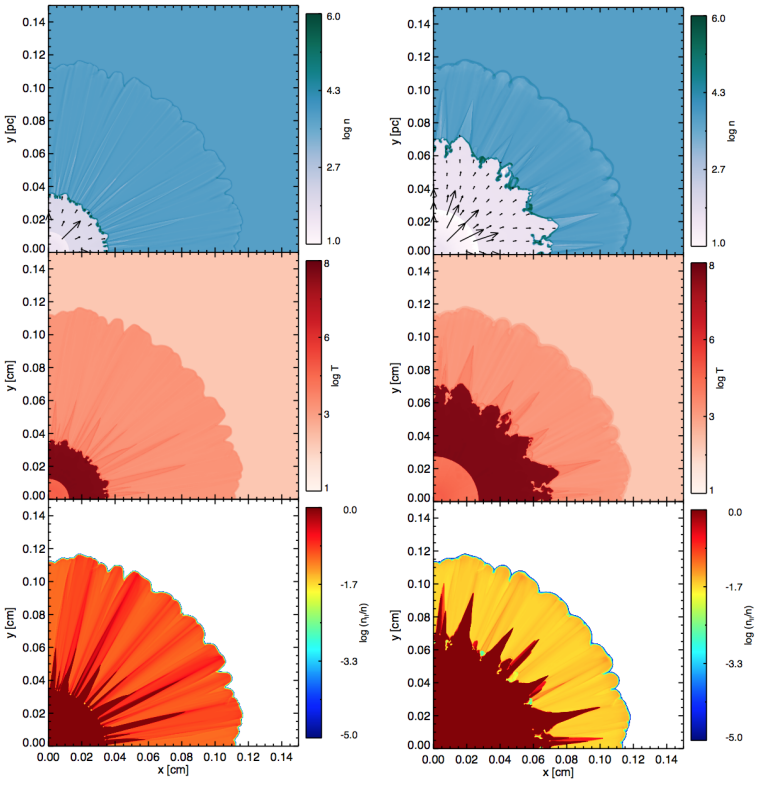

(a) 200 yr (b) 500 yr

Figure 2.16 – Number density together with the velocity field (top), gas temperature (middle), and degree of hydrogen ionization (bottom) for the stellar wind model at age (a) 200 yr, and (b) 500 yr with level of refinement up to 8. The star is located at the center of the coordinate system.

The swept-up shell has the same instability modes at both levels of refinement. The structures visible at refinement level 9 can be matched to the one at refinement 8. The energetics involved in the problem do not change with resolution giving us confidence that choosing refinement level 8 is a good compromise between computational cost and level of details reached in the simulation.

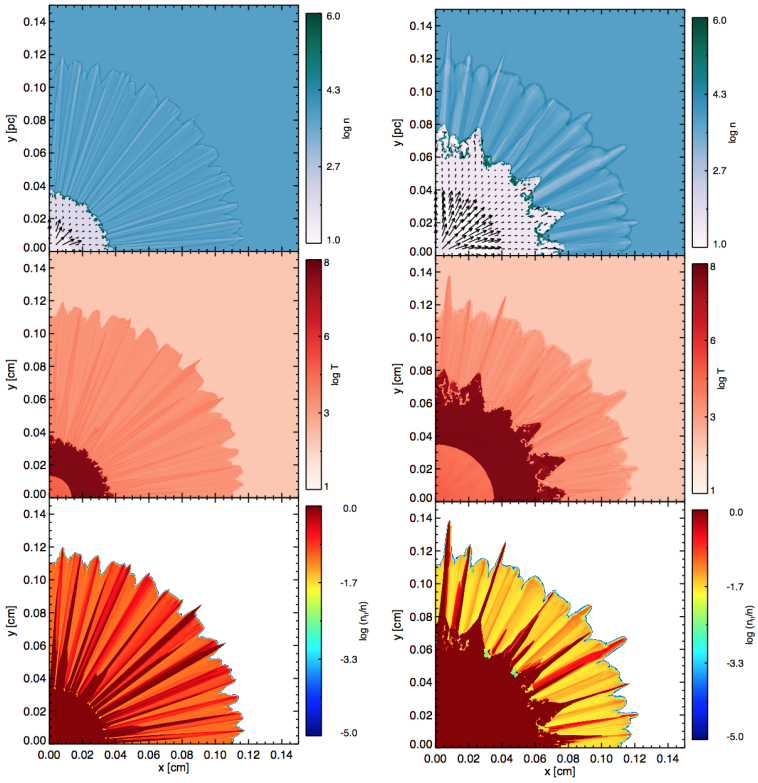

(a) 200 yr (b) 500 yr

Figure 2.17 – Number density together with the velocity field (top), gas temperature (middle), and degree of hydrogen ionization (bottom) for the stellar wind model at age (a) 200 yr, and (b) 500 yr with level of refinement up to 9. The star is located at the center of the coordinate system.